




Cite this: *Mater. Adv.*, 2021,
2, 6988

Received 31st August 2021,
Accepted 30th September 2021

DOI: 10.1039/d1ma00783a

rsc.li/materials-advances

Controlling the size and circular dichroism of chiral gold helicoids†

Jeong Won Kim,* Nam Heon Cho,* Yae-Chan Lim,* Sang Won Im,
Jeong Hyun Han and Ki Tae Nam *

The precise control of size and optical response holds significance in various applications, but the detailed control of the contributing electric dipole and magnetic dipole to tune the chiroptic response remains a challenge. In this work, we systematically controlled the size- and optical-properties of chiral gold 432 helicoid III nanoparticles using an aqueous-based seed-mediated method. Control of the Au metal precursor and glutathione concentration yields various sizes of chiral nanoparticles with a precisely controlled geometry from 100 nm to 180 nm and maximum chiroptic peak positions from 540 nm to 650 nm. Based on this synthetic platform, a comprehensive understanding of chiral morphology, optical response, and the corresponding simulation data has been developed.

Introduction

Chiral materials possess great importance, not only in fundamental physics but also in practical applications. The definition of a chiral object is that it is non-superimposable on its mirror image, *i.e.*, two objects with opposite handedness exhibit different physical properties despite having identical components. These chiral structures can be distinguished by their selective optical response to circularly polarized light, altering the polarization state of light or elliptically modulating incoming linearly polarized light. In order to fully utilize this optical activity, using plasmonic materials with inherently strong light-matter interactions for the construction of chiral nanomaterials has been highlighted.^{1–7} Considering that chiral plasmonic nanostructures with various shapes and physical dimensions offer versatility to the chiroptic response, a synthetic platform for the sophisticated control of nanoscale chirality is required. Given that the shape and physical dimensions of chiral plasmonic nanostructures play a critical role in obtaining a desired optical response, precise control over the size and morphology of a

chiral plasmonic nanomaterial using various artificial synthesis methods has been suggested.^{8–12}

In 2018, our group demonstrated the aqueous-based seed-mediated chemical synthesis of 3-dimensional chiral nanoparticles using thiol-containing amino acids and peptides.¹³ The 432 helicoid III nanoparticles, named after their 4-, 3-, and 2-fold rotational symmetry, utilize the enantioselective adsorption of chiral peptides such as glutathione (GSH) to the generated high-index planes of gold nanoparticles. Such enantioselective adsorption induces the dominant development of $^S\{hkl\}$ surfaces using L-GSH while using D-GSH induces the dominant development of $^R\{hkl\}$ surfaces. The devised synthetic method demonstrated various nanoparticle morphologies and chiroptic responses,^{14,15} which through systematic optimization of the synthetic conditions enhanced the *g*-factor up to 0.3.¹⁶ However, control over the nanoparticle size and maximum chiroptic peak position was limited to a fixed size and wavelength. Therefore, we believe that synthetic efforts to precisely control the size and spectral position of 432 helicoid III could significantly broaden the range of applications to include size-sensitive or spectral-sensitive nanoparticle applications such as cellular interaction studies or broadband optical communication systems.^{17–20}

Herein, we have directly distinguished the exact role of the Au metal ion precursor and GSH molecule in the evolution of the chirality to control the size and optical response of 432 helicoid III. Under a specific ratio of Au precursor to GSH, control of the total Au precursor concentration controlled the size of chiral nanoparticles from 100 nm to 180 nm while maintaining efficient evolution of the chirality. Size-controlled 432 helicoid III shows a gradual change in size and chiral gap structures, where this change in chiral-gap morphology has been directly correlated with the increase and spectral shift of the chiroptic response. We expect that this change in chiroptic response is highly likely to arise from the generation of electric dipole and magnetic dipole modes from the change in gap structures, and further numerical mode-analysis has been conducted to confirm this. We believe that this study demonstrates precise control over the size and chiroptic response of

Department of Materials Science and Engineering, Seoul National University,
Seoul 08826, Republic of Korea. E-mail: nkitae@snu.ac.kr

† Electronic supplementary information (ESI) available. See DOI: 10.1039/d1ma00783a

our 432 helicoid III nanoparticles and further signifies the importance of chiral-gap structures in the generation of an exceptional chiroptic response.

Experimental section

Materials

The following chemical products were purchased and used without further purification: hexadecyltrimethylammonium bromide (CTAB) (99%, Acros), hexadecyltrimethylammonium chloride (98%, Aldrich), L-ascorbic acid (99%, Aldrich), tetrachloroauric(III) trihydrate (99.9%, Aldrich), sodium tetrahydridoborate (99%, Aldrich), potassium iodide (99.5%, Aldrich), and L-glutathione (98%, reduced, Aldrich). All aqueous solutions were prepared using high-purity deionized water ($18.2 \text{ M}\Omega \text{ cm}^{-1}$).

Synthesis of size-controlled 432 helicoid III nanoparticles

Octahedral seed nanoparticles were synthesized as reported previously.²¹ Before use, the seed nanoparticles were centrifuged (12 000 rpm, 3 min) and dispersed in 1 mM CTAB aqueous solution. The growth solution for the 432 helicoid III nanoparticles of different sizes was prepared by adding 800 μL of 100 mM CTAB and 100 μL of various concentrations of gold chloride trihydrate to 3.95 mL of deionized water. By the rapid injection of 475 μL of 100 mM ascorbic acid solution, the reduction of Au^{3+} was initiated. Then, the growth of gold nanoparticles was initiated by adding 5 μL of various concentrations of L-GSH (GSH) followed by the addition of 50 μL of octahedral seed solution to the growth solution. The growth solution was incubated for 2 h in a 30 °C water bath. The solution was centrifuged three times (6000 rpm 1 min) and re-dispersed in 1 mM CTAB aqueous solution.

Characterization

Circular dichroism (CD) spectra were obtained using a J-815 spectropolarimeter (JASCO) and extinction spectra were obtained using a UV-vis spectrophotometer (Agilent). Kuhn's dissymmetry factor (*g*-factor) was calculated from the measured CD value and extinction using the following equation:

$$g\text{-factor} = 2 \frac{A_L - A_R}{A_L + A_R}$$

For structural analysis, scanning electron microscopic (SEM) images were taken using a SUPRA 55VP instrument (Zeiss).

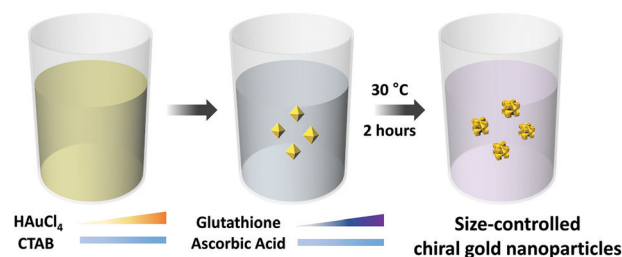
Numerical calculations

The optical simulation was conducted using a commercial Maxwell equation solver based on the finite element method (COMSOL). The simulation domain was composed of a spherical core-shell structure, where the calculation domain was enclosed by the perfectly matched layer absorbing the residual electromagnetic field. The gold nanoparticle structure was placed in a water medium with a refractive index of 1.33. To examine the experimental absorbance data, the extinction cross-section was

calculated by addition of the scattering and absorption cross-sections. The scattering cross-section was obtained from the surface integration of the scattered Poynting vectors for the spherical boundary in the calculation domain, and the absorption cross-section was calculated by the volume integration of the resistive losses inside the sample geometry. The multipole coefficients were calculated from the multipole expansion of the electromagnetic field in terms of vector spherical harmonic wavefunctions, and each multipole's contribution to the extinction cross-section was calculated by assuming that an x-polarized plane wave was incident.²²

Results and discussion

In terms of controlling the nanoparticle size during the seed-mediated method, three possible ways could be attempted: (1) control of the pre-synthesized seed nanoparticle size, (2) control of the nanoparticle growth time, and (3) control of the total Au precursor concentration. Decreasing of the pre-synthesized seed nanoparticle size resulted in less defined facet generation, which decreased the uniformity of the final nanoparticles. Reduction of the synthesis time resulted in relatively less defined chiral-gap formation due to insufficient growth of the stable cubical boundary.¹⁶ Therefore, in order to uniformly control the 432 helicoid III nanoparticle size while maintaining the representative chiral structures, the total Au precursor concentration and GSH concentration were systematically altered. The experimental scheme of the size-controlled 432 helicoid III synthesis is shown in Scheme 1 and detailed synthetic conditions are mentioned in the Experimental section. The HAuCl_4 metal ion precursor (Au precursor) was added to the prepared CTAB solution to form the $[\text{AuBr}_4]^-$ complex. Upon addition of the reducing agent (ascorbic acid), Au^{3+} is reduced to Au^0 , which shows a distinct colour transition from yellow to a transparent colour. Then, after the addition of the chirality-inducing glutathione molecule, nanoparticle growth was initiated *via* the injection of pre-synthesized gold octahedral seed nanoparticles. The reaction proceeded at 30 °C for 2 hours,



Scheme 1 Synthesis of size-controlled 432 helicoid III nanoparticles. Schematic illustration of the synthesis of size-controlled 432 helicoid III nanoparticles. Modification of gold precursor and GSH concentrations controls the size and growth direction of chiral nanoparticles grown from octahedral seeds. CTAB and ascorbic acid were introduced to the growth solution as a surfactant and a reducing agent, respectively. Triangular bars with colour gradation were used to express the concentration variation of gold precursor and GSH concentrations.



then nanoparticle solutions were centrifuged to be collected for further characterization.

Independent control of the total Au precursor and GSH concentrations induced an optical and morphological change in the nanoparticles, which was observed using CD and SEM measurements as shown in Fig. 1A–D. In Fig. 1A, the chiroptic response of the chiral nanoparticles with variation in the Au precursor concentration from 50 μM to 400 μM is shown. The g -factor was calculated using the above-mentioned equation, based on the measured CD and extinction data as shown in Fig. S1 (ESI[†]). The generated chiroptic response shows a gradual redshift of the maximum chiroptic spectral position from 560 nm to 770 nm while the maximum g -factor of around 0.2 was reached at 200 μM . The existence of an optimum gold concentration for the highest chiroptic response is observed since a gold precursor concentration of more than 200 μM induces a decrease of the chiroptic response with a consistent redshift trend of the maximum peak position. The size and morphological change due to variation of the gold precursor is shown in Fig. 1C. While gold nanoparticles synthesized using 50 μM of Au precursors show a significantly smaller size with no observable chiral morphology but only high-index facets, the nanoparticles start to show an increase in size and the development of a chiral morphology with a curved gap structure as the Au precursor concentration is increased up to 200 μM .

A further increase of the Au precursor concentration towards 400 μM gradually increases the size of the nanoparticles but they develop irregularly shaped chiral-gap structures. Based on our result of the optimum gold precursor concentration being 200 μM , the effect of varying the GSH concentration on the chirality development was investigated. As shown in Fig. 1B, a steep incline of the chiroptic response with a maximum g -factor of around 0.2 with a consistent redshift of the maximum peak position was observed on increasing the GSH concentration from 1.4 μM to 5.5 μM . Further increasing the GSH concentration from 5.5 μM to 11 μM reduces the g -factor value from 0.2 to 0.05, while showing the irregular movement of the maximum chiroptic peak position. As shown in Fig. 1D, when the GSH concentration of 1.4 μM was used, only a shallow gap formation with a cubic boundary was observed. With the gradual increase of the concentration to 5.5 μM , the cubic outer boundaries with an engraving of defined chiral gap structures are generated. However, further increasing the GSH concentration to 11 μM shows a nanoparticle morphology with non-cubic outer boundaries and malformed chiral-gap structures.

From independently varying the Au precursor concentration and GSH concentration, the exact role of each reagent on the chirality evolution was distinguished. Increasing the Au precursor concentration controls the nanoparticle size and induces a redshift of the chiroptic peak position. Increasing

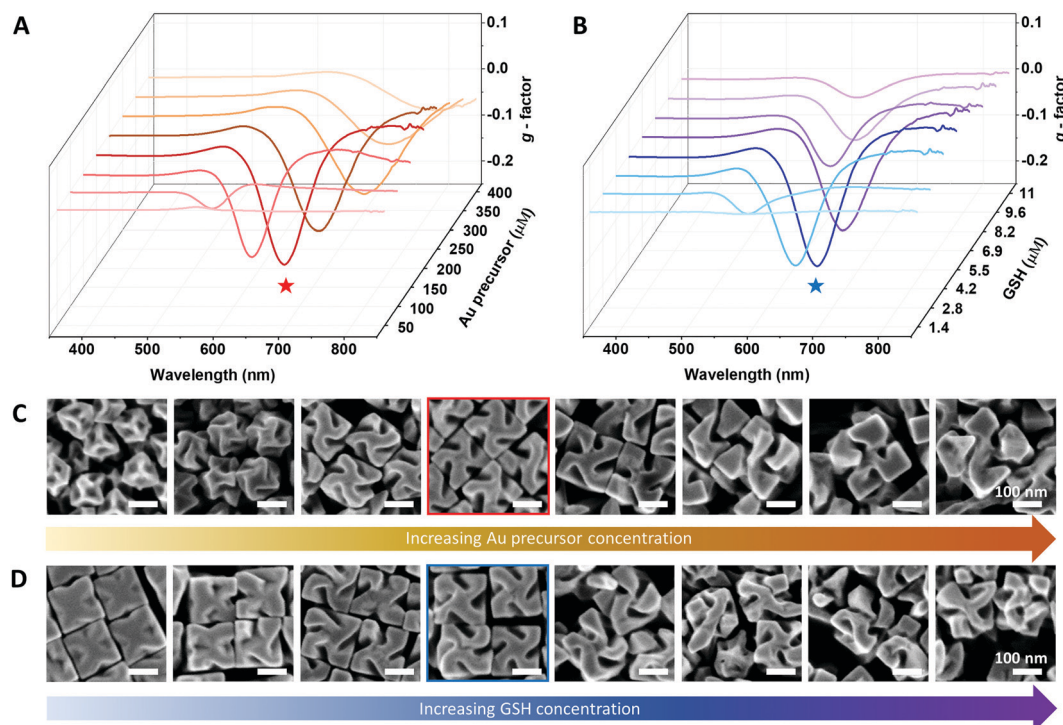


Fig. 1 Effect of Au precursor and GSH concentration on the chirality development of 432 helicoid III nanoparticles. (A) Chiroptic response of 432 helicoid III with respect to variation of the Au precursor concentration. The GSH concentration is constant at 5.5 μM . (B) Chiroptic response of 432 helicoid III with respect to variation of the GSH concentration, while the Au precursor concentration is kept as 200 μM . (C) Corresponding SEM images of 432 helicoid III nanoparticles synthesized by varying the Au precursor concentration. (D) Corresponding SEM images of 432 helicoid III nanoparticles synthesized by varying the GSH concentration. The optimum chiroptic responses are marked with stars and the corresponding SEM images are denoted as outlined boxes with each corresponding color of the star. (A and C) Au precursor concentrations: 50 μM , 100 μM , 150 μM , 200 μM , 250 μM , 300 μM and 400 μM . (B and D) GSH concentrations: 1.4 μM , 2.8 μM , 4.2 μM , 5.5 μM , 6.9 μM , 8.2 μM , 9.6 μM and 11 μM .



the GSH concentration induced a complex effect as it controlled the magnitude of chirality development, which also affected the spectral position while not changing the particle edge length. The exact roles of the Au precursor and GSH concentrations found here are in good agreement with our conventional understanding of their role in chirality development, with the Au precursor dictating the absolute amount of gold atoms being deposited and the GSH molecule dictating the location of atom deposition onto the seed nanoparticle for the chiral-morphology development.¹⁶ From the above experiment, controlling the synthetic parameters showed an optimum relative ratio, bringing about the most efficient chirality development with the highest chiroptic response. Therefore, we suggest control of the 432 helicoid III nanoparticle size and optical response by maintaining a specific ratio of Au precursor:GSH to 36:1, calculated from the optimum concentration, while controlling the total amount of Au precursor concentration.

With maintaining the specific Au-to-GSH concentration ratio of 36:1, Au concentrations were controlled from 60 μM and 200 μM in increments of 20 μM to specifically control the size of the 432 helicoid III nanoparticles. The size-controlled 432 helicoid III nanoparticles show an edge length of 90 nm, 100 nm, 110 nm, 120 nm, 140 nm, 150 nm, 160 nm and 180 nm with respect to the Au precursor concentration change. Representatively, Fig. 2A and B clearly show the difference in chiral morphology development of size-controlled 432 helicoid III nanoparticles with the uniform controllability of the developmental stage and size of the chiral nanomaterial through variation of the Au concentration between 80 μM and 200 μM . The 432 helicoid III synthesized with 80 μM yields the final edge-length size of 100 nm with growth up to the generation of the representative chiral gap structures. However, 432 helicoid III nanoparticles synthesized

using 200 μM show a 180 nm edge length with the uniform generation of the stable (100) facet and cubic outer boundary with the formation of a defined chiral-gap structure.

The different stages of chirality development with respect to the size control of 432 helicoid III is more clearly shown in Fig. 2C. From our previous understanding of the 432 helicoid III growth pathway, the development of chirality is clearly distinguished into two growth regimes.²³ While the initial nanoparticle growth region proceeds towards high-index formation accompanied with a chiral motif generation, the second nanoparticle growth region extends its growth up to the chiral-gap formation accompanied with stabilization of the (100) facet with a cubical boundary. As shown in Fig. 2C, a 90 nm-sized nanoparticle shows a minimal generation of the chirality while 100 nm 432 helicoid III nanoparticles start to form the representative chiral motif structures. A further size increase to 110 nm 432 helicoid III nanoparticles shows the transition of the growth regime from chiral motif generation to (100) facet stabilization, which induces the transformation of chiral motifs to chiral-gap structures with a cubic outer boundary. However, for the 120 nm size 432 helicoid III and above, the nanoparticles show a gradual increase in size while the chiral-gap structure remains relatively similar for all. Quantitative comparison of the detailed gap geometry between the 120-nm-sized 432 helicoid III and the 180-nm-sized 432 helicoid III nanoparticles showed that the dominant change of the gap structure occurs in the gap depth. As shown in Table S1 (ESI[†]), 50 nanoparticles of each size were measured according to the geometric parameters of nanoparticle size, gap depth, gap angle, and gap width. The 120 nm and 180 nm 432 helicoid III nanoparticles show a significant increase in gap depth from 56.2 nm to 71.3 nm, while the gap width and gap angle showed

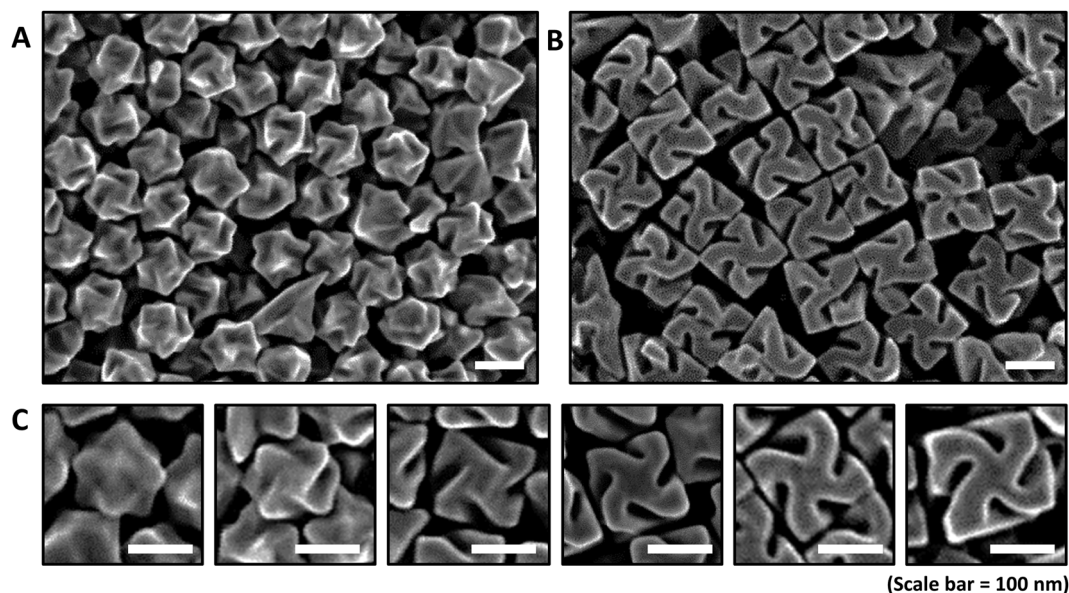


Fig. 2 Chiral morphology of size-controlled 432 helicoid III nanoparticles. Chiral morphology development and size growth of 432 helicoid III nanoparticles. Low-magnification SEM images of (A) 432 helicoid III nanoparticles with a 100 nm edge length and (B) 432 helicoid III nanoparticles with a 180 nm edge length. (C) High-magnification SEM images showing the chiral-morphology development of single 432 helicoid III nanoparticles. From left to right, 90 nm, 100 nm, 110 nm, 120 nm, 150 nm and 180 nm sized 432 helicoid III nanoparticles.



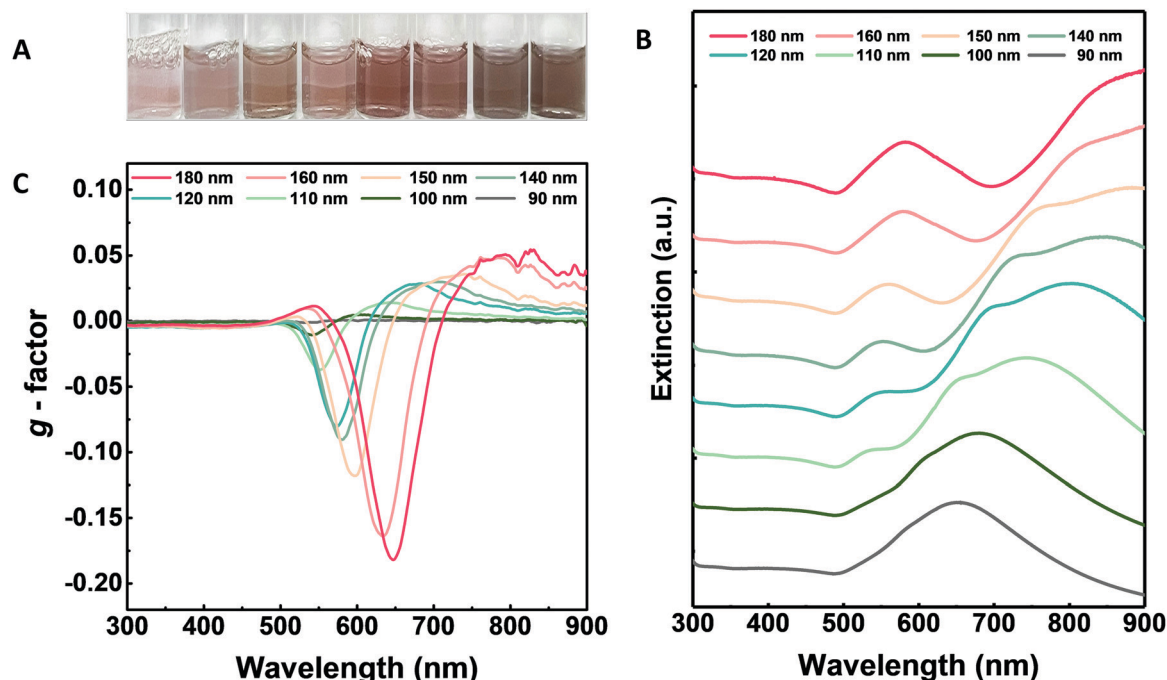


Fig. 3 Optical characterization of size-controlled 432 helicoid III nanoparticles. (A) Colours of 432 helicoid III nanoparticles with different sizes synthesized by controlling the Au precursor and GSH molecule concentrations. From left to right, 432 helicoid III sizes increased from 90 nm to 180 nm. (B) Extinction spectra of size-controlled 432 helicoid III nanoparticles showing the development of two representative peaks as the size of the nanoparticles increases. The extinction peak located near 550 nm and the shoulder peak in the longer wavelength range started to appear from 100 nm 432 helicoid III nanoparticles. (C) *g*-Factor spectra of size-controlled 432 helicoid III nanoparticles.

a marginal change from 21.5 nm to 23.8 nm and 44.0° to 49.7°, respectively. From this result, it is possible to conclude that the edge length and the gap depth show the most significant change in dimension as the nanoparticle size increases. Considering that our previous simulation data for 432 helicoid III nanoparticles with different geometries predicts that the gap depth and the edge length most dominantly affect the chiroptic response, a significant chiroptic response change can be expected from size-controlled 432 helicoid III nanoparticles.¹³

Based on our analysis of the nanoparticle size and gap-structure variation, the direct correlation between the structural chirality and its optical response needs to be further investigated. As shown in Fig. 3A, nanoparticles with different sizes and gap structures exhibit significantly different solution colours and transparencies. As the nanoparticle size increases, the solution colour changes from transparent pink to opaque dark brown. This visible colour change clearly implies the subsequent spectral change with respect to the nanoparticle size variation. As shown in Fig. 3B, a single extinction peak near 650 nm was observed for the 90 nm 432 helicoid III nanoparticles without a chiral gap structure. As the gap develops with the increase in the size of the nanoparticles, the extinction spectrum of the size-controlled 432 helicoid III nanoparticles shows the generation of two new peaks, which gradually become more distinct, while 110-nm-sized 432 helicoid III starts to show a slight peak generation at 540 nm and a shoulder peak at 650 nm. In terms of the peak generated at 540 nm, with respect to the gradual size increase of the nanoparticles to 120 nm, 140 nm, 150 nm, 160 nm and 180 nm, this

results in elevation of the peak with a marginal spectral position shift from 550 nm to 580 nm. Furthermore, with the increase in nanoparticle size, a more distinct redshift trend of the extinction peak position is observed. At the nanoparticle size of 120 nm, the original shoulder peak and the extinction peak at 650 nm are now shifted, with the shoulder peak being near 700 nm and the original peak at 650 nm shifting to 800 nm. This significant redshift of spectral position in the shoulder and the original extinction peak continues further, with the spectral shift of the shoulder peak from 730 nm to 770 nm for 140- and 150-nm-sized 432 helicoid III nanoparticles and the original extinction peak from 800 nm to the NIR region, respectively. Finally, the 180-nm-sized 432 helicoid III nanoparticles show three distinct extinction peaks generated at 580 nm, near 800 nm, and above 900 nm. A subsequent change in the optical response due to variation of the size and gap-structure generation is also shown in the chiroptic response development shown in Fig. 3C. As the nanoparticle size increases, the absolute *g*-factor of the 432 helicoid III nanoparticles increases from 0.04 to 0.2, with a clear spectral shift of the maximum chiroptic peak position from 540 nm to 650 nm. Compared with most reported chiral nanostructures, which show the chiroptic response of the *g*-factor around the 10^{-2} scale in the visible wavelength region, the size-controlled 432 helicoid III nanoparticles – with precise chiroptic response modulation up to a *g*-factor of the 10^{-1} scale – offer distinguishable engineering and scientific advantages.^{8,12,24–26}

From a theoretical perspective, the chiroptic response can be interpreted as interference of the electric dipole (ED) and the



magnetic dipole moment (MD) induced by the electromagnetic field.^{27–29} In detail, the induced ED is aligned parallel to the electric field, while the MD is barely generated from the magnetic field but is mainly formed from an induced current loop in curved surfaces. Considering the geometry of the size-controlled 432 helicoid III nanoparticles that have carved chiral-gap structures with a cubic outer boundary, the chiral surface in the gap morphology can serve as a site where MD resonance can occur. Based on this analogy, a strong chiroptic response ranging from 540 to 650 nm can indicate the generation of ED and MD modes in the chiral gap surface within the same wavelength region. Furthermore, generation of the extinction peak starting near 550 nm can also be expected to be gap-related ED and MD resonance peaks, considering that its evolution began simultaneously with the increased gap depth and enhancement of the chiroptic response. The spectral position change of the chiroptic response can also be understood using a similar analogy. Considering that the ED component is strictly related to the entire volume of the nanoparticle and the magnetic dipole mode is known to be confined in the gap structures, the spectral shift of the shoulder peak and original peak from 650 nm is expected to be from ED and other higher modes generated. Furthermore, considering that the spectral shift of the chiroptic response occurs in accordance with the change in the gap structure, we also expect that the MD component shows the dominant effect. To fully support our integration of correlation between the chiral-gap structure and its chiroptic and extinction spectra, in-depth numerical mode analysis of constructed models was conducted.

The numerical simulation using the finite element method-based Maxwell equation solver (COMSOL) was conducted using the 100 nm, 120 nm, 140 nm, 160 nm and 180-nm-sized 432 helicoid III structures. Graphical modelling of the simulated size-controlled nanoparticles and the detailed numerical-calculation methodology is shown in the Experimental section and the ESI† in Fig. S2. Briefly, a single nanoparticle was placed at the centre of the calculation domain and x-polarized plane-wave excitation was applied. For evaluation of the optical responses of each nanoparticle, the extinction cross-section was calculated by adding the absorption and scattering cross-sections of the nanoparticle. This simulation study theoretically supports our current understanding of the direct relationship between the change in morphology and the respective change in optical response.

Simulated extinction spectra and multipole analysis of the size-controlled 432 helicoid III nanoparticles are shown in Fig. 4A–F. In Fig. 4A, 100-nm-sized 432 helicoid III nanoparticles with only the chiral motif structure show a single peak generation, while the 120-nm-sized 432 helicoid III shows the evolution of a 550 nm peak and a shoulder peak near 700 nm. Further increase of the nanoparticle size shows a clear trend of a red shift in the spectral position of the shoulder peak as well as in the original peak at 630 nm, which is in great accordance with experimental data. The multipole analysis results shown in Fig. 4B–F revealed that this new peak consists of multiple modes generated, including the magnetic dipole mode. These results clearly show that a 550 nm peak arises as a result of the inclusion of chiral gap structures with magnetic dipole resonance. Furthermore, the size-controlled 432 helicoid

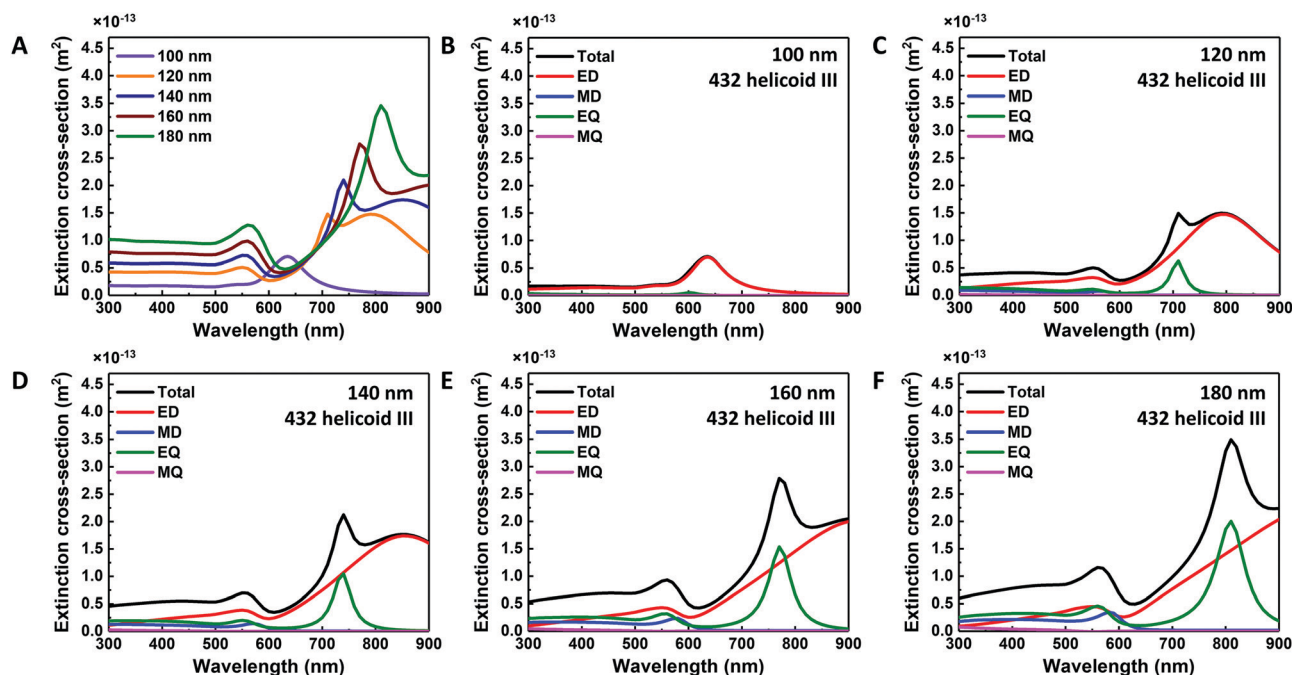


Fig. 4 Mode analysis of size-controlled 432 helicoid III nanoparticles. (A) Extinction cross-section of 432 helicoid III nanoparticles with variation in size and morphology. Multipole analysis of (B) 100 nm 432 helicoid III, (C) 120 nm 432 helicoid III, (D) 140 nm 432 helicoid III, (E) 160 nm 432 helicoid III, and (F) 180 nm 432 helicoid III nanoparticles.



III nanoparticles show that the original single extinction peak, mainly of ED, gradually diverges into a mixture of ED, MD and EQ. With the increase in nanoparticle size, the ED and EQ modes show a clear spectral redshift, which indicates that size variation and the spectral redshift could be more dominantly related to electric modes. Additionally, the distinct shoulder-peak generation observed in experiments shows high accordance with the simulated EQ mode in terms of the peak position. The multipole modes in the 432 helicoid III nanoparticles could further variate its utilization, as the MD component for magnetic applications or the EQ component for orbital angular momentum applications, as previously suggested.^{30–34}

The origin of the increase in chiroptic response intensity and spectral shift with respect to the size variation was also studied. As expected, in the multipole analysis of size-controlled 432 helicoid III structures, starting from the nanoparticle size of 120 nm, which has the defined chiral gap, the MD component increases in its intensity as the nanoparticle size increases. Furthermore, the spectral shift of chiroptic response could also be understood from the change in the MD mode. Experimentally, the increase of nanoparticle size induced a gradual spectral shift to the maximum chiroptic response. From the simulation data, with the increase of nanoparticle size, the ED component shows a constant spectral position at 550 nm. However, the MD component shows gradual spectral position change with respect to increase of nanoparticle size in which 120 nm, 140 nm, 160 nm and 180-nm-sized 432 helicoid III nanoparticles showed an MD peak position of 560 nm, 570 nm, 580 nm, and 580 nm, respectively. With respect to this spectral position change, the simulated chiroptic response data also show a gradual shift of the maximum chiroptic peak position from 570 nm to 590 nm, as shown in Fig. S3 (ESI[†]), which is in accordance with our experimental data in terms of the spectral peak movement. These results coincide with the increase and the spectral shift of the chiroptic response explained in terms of the chiral gap from the size-controlled 432 helicoid III nanoparticles. From the correlation between the experimental and the simulation data, the importance of defined chiral-gap formation is shown for the systematic modulation of the chiroptic response in 432 helicoid III nanoparticles.

Conclusions

In summary, we have systematically controlled the nanoparticle size and chiroptic response of 432 helicoid III nanoparticles with an edge-length size variation from 100 nm to 180 nm and a maximum chiroptic peak position shift that ranges from 540 nm to 650 nm. Based on the detailed synthetic justification of roles of the Au precursor and GSH molecules during chirality evolution, size variation of 432 helicoid III nanoparticles was conducted by controlling the total Au precursor concentration while Au precursor-to-GSH concentration ratio was kept constant under optimized conditions. Comprehensive understanding of the size-controlled 432 helicoid III structures from the direct

correlation of their morphology development to optical response development indicated the significance of the chiral-gap formation on the evolution of the chiroptic response and the change in the extinction spectra. Based on the electromagnetic understanding of chirality, the origin of the above-mentioned optical response change due to the nanoparticle size is specifically attributed to the generation of the MD mode from chiral-gap structures. Furthermore, numerical simulation data show clear coinciding data compared to experimental data and analysis, in which multiple modes were generated with respect to the nanoparticle size increase, and the strong MD mode was generated at the complex chiral gap morphology. We believe that our current work holds two significant implications: (1) the experimental demonstration of precise chiral nanomaterial size and optical-response tuning, and (2) the theoretical interpretation of experimental data that clearly suggest the possible origin of such a strong and dynamically changed optical response. These results not only broaden our spectrum for potential applicability but enhance our understanding of the design principles of chiral nanomaterials from a theoretical perspective.

Author contributions

K. T. N. conceived and supervised the project. J. W. K., N. H. C., and Y.-C. L. contributed equally. J. W. K. and N. H. C. designed the experiments, characterized the materials, and wrote the manuscript. Y.-C. L. conducted the numerical simulation and wrote the manuscript. S. W. I. constructed the 3D models and conducted the morphology analysis. J. H. H. synthesized the nanomaterials. All authors discussed the experiments and contributed to writing the manuscript. K. T. N. wrote the manuscript and guided all aspects of the work.

Conflicts of interest

There are no conflicts to declare.

Acknowledgements

This research was supported by the Defense Challengeable Future Technology Program of the Agency for Defense Development, Republic of Korea. This research was supported by the Creative Materials Discovery Program through the National Research Foundation of Korea (NRF) funded by the Ministry of Science and ICT (NRF-2017M3D1A1039377). KTN appreciates the support from the Institute of Engineering Research, Research Institute of Advanced Materials (RIAM) and Soft Foundry at Seoul National University.

Notes and references

- 1 J. Liu, L. Yang, P. Qin, S. Zhang, K. K. L. Yung and Z. Huang, *Adv. Mater.*, 2021, 2005506.
- 2 M. Hentschel, M. Schäferling, X. Duan, H. Giessen and N. Liu, *Sci. Adv.*, 2017, 3, e1602735.



- 3 J. T. Collins, C. Kuppe, D. C. Hooper, C. Sibilía, M. Centini and V. K. Valev, *Adv. Opt. Mater.*, 2017, **5**, 1700182.
- 4 H. Kim, S. W. Im, R. M. Kim, N. H. Cho, H.-E. Lee, H.-Y. Ahn and K. T. Nam, *Mater. Adv.*, 2020, **1**, 512–524.
- 5 H.-Y. Ahn, S. Yoo, N. H. Cho, R. M. Kim, H. Kim, J.-H. Huh, S. Lee and K. T. Nam, *Acc. Chem. Res.*, 2019, **52**, 2768–2783.
- 6 C.-W. Lee, H. J. Choi and H. Jeong, *Nano Convergence*, 2020, **7**, 3.
- 7 Y. Chen, B. Ai and Z. J. Wong, *Nano Convergence*, 2020, **7**, 18.
- 8 A. Guerrero-Martínez, B. Auguie, J. L. Alonso-Gómez, Z. Džolić, S. Gómez-Graña, M. Žinić, M. M. Cid and L. M. Liz-Marzán, *Angew. Chem., Int. Ed.*, 2011, **50**, 5499–5503.
- 9 J. Lu, Y. Xue, K. Bernardino, N.-N. Zhang, W. R. Gomes, N. S. Ramesar, S. Liu, Z. Hu, T. Sun, A. F. de Moura, N. A. Kotov and K. Liu, *Science*, 2021, **371**, 1368–1374.
- 10 W. Yan, L. Xu, C. Xu, W. Ma, H. Kuang, L. Wang and N. A. Kotov, *J. Am. Chem. Soc.*, 2012, **134**, 15114–15121.
- 11 G. González-Rubio, J. Mosquera, V. Kumar, A. Pedrazo-Tardajos, P. Llombart, D. M. Solís, I. Lobato, E. G. Noya, A. Guerrero-Martínez, J. M. Taboada, F. Obelleiro, L. G. MacDowell, S. Bals and L. M. Liz-Marzán, *Science*, 2020, **368**, 1472–1477.
- 12 A. Ben-Moshe, S. G. Wolf, M. B. Sadan, L. Houben, Z. Fan, A. O. Govorov and G. Markovich, *Nat. Commun.*, 2014, **5**, 4302.
- 13 H.-E. Lee, H.-Y. Ahn, J. Mun, Y. Y. Lee, M. Kim, N. H. Cho, K. Chang, W. S. Kim, J. Rho and K. T. Nam, *Nature*, 2018, **556**, 360–365.
- 14 H. Kim, S. W. Im, N. H. Cho, D. H. Seo, R. M. Kim, Y. Lim, H. Lee, H. Ahn and K. T. Nam, *Angew. Chem., Int. Ed.*, 2020, **59**, 12976–12983.
- 15 H.-E. Lee, R. M. Kim, H.-Y. Ahn, Y. Y. Lee, G. H. Byun, S. W. Im, J. Mun, J. Rho and K. T. Nam, *Nat. Commun.*, 2020, **11**, 263.
- 16 N. H. Cho, G. H. Byun, Y.-C. Lim, S. W. Im, H. Kim, H.-E. Lee, H.-Y. Ahn and K. T. Nam, *ACS Nano*, 2020, **14**, 3595–3602.
- 17 K. Aydin, V. E. Ferry, R. M. Briggs and H. A. Atwater, *Nat. Commun.*, 2011, **2**, 517.
- 18 N. Hoshyar, S. Gray, H. Han and G. Bao, *Nanomedicine*, 2016, **11**, 673–692.
- 19 B. D. Chithrani and W. C. W. Chan, *Nano Lett.*, 2007, **7**, 1542–1550.
- 20 Y. Zhao, M. A. Belkin and A. Alù, *Nat. Commun.*, 2012, **3**, 870.
- 21 H.-L. Wu, H.-R. Tsai, Y.-T. Hung, K.-U. Lao, C.-W. Liao, P.-J. Chung, J.-S. Huang, I.-C. Chen and M. H. Huang, *Inorg. Chem.*, 2011, **50**, 8106–8111.
- 22 P. Grahm, A. Shevchenko and M. Kaivola, *New J. Phys.*, 2012, **14**, 093033.
- 23 N. H. Cho, G. H. Byun, Y.-C. Lim, S. W. Im, H. Kim, H.-E. Lee, H.-Y. Ahn and K. T. Nam, *ACS Nano*, 2020, **14**, 3595–3602.
- 24 X. Wu, L. Xu, W. Ma, L. Liu, H. Kuang, N. A. Kotov and C. Xu, *Adv. Mater.*, 2016, **28**, 5907–5915.
- 25 C. Hao, L. Xu, W. Ma, X. Wu, L. Wang, H. Kuang and C. Xu, *Adv. Funct. Mater.*, 2015, **25**, 5816–5822.
- 26 X. Wu, L. Xu, L. Liu, W. Ma, H. Yin, H. Kuang, L. Wang, C. Xu and N. A. Kotov, *J. Am. Chem. Soc.*, 2013, **135**, 18629–18636.
- 27 L. Hu, Y. Huang, L. Pan and Y. Fang, *Sci. Rep.*, 2017, **7**, 11151.
- 28 A. O. Govorov, Z. Fan, P. Hernandez, J. M. Slocik and R. R. Naik, *Nano Lett.*, 2010, **10**, 1374–1382.
- 29 D. L. Jaggard, A. R. Mickelson and C. H. Papas, *Appl. Phys.*, 1979, **18**, 211–216.
- 30 C. T. Schmiegelow, J. Schulz, H. Kaufmann, T. Ruster, U. G. Poschinger and F. Schmidt-Kaler, *Nat. Commun.*, 2016, **7**, 12998.
- 31 A. J. Silenko, P. Zhang and L. Zou, *Phys. Rev. Lett.*, 2019, **122**, 063201.
- 32 F. Pineider, G. Campo, V. Bonanni, C. de Julián Fernández, G. Mattei, A. Caneschi, D. Gatteschi and C. Sangregorio, *Nano Lett.*, 2013, **13**, 4785–4789.
- 33 O. H.-C. Cheng, D. H. Son and M. Sheldon, *Nat. Photonics*, 2020, **14**, 365–368.
- 34 P. Dong, E. A. Fisher, M.-V. Meli and S. Trudel, *Nanoscale*, 2020, **12**, 19797–19803.

